A high pressure, high temperature gas medium apparatus to measure acoustic velocities during deformation of rock

C. Harbord, N. Brantut, E. C. David, et al.

View Online   Export Citation   CrossMark

ARTICLES YOU MAY BE INTERESTED IN

Read Now!

Review of Scientific Instruments

Special Issue: Advances in Measurements and Instrumentation Leveraging Embedded Systems

AIP Publishing

93, 053908

A high pressure, high temperature gas medium apparatus to measure acoustic velocities during deformation of rock

View Online   Export Citation   CrossMark

C. Harbord,[a] N. Brantut, E. C. David, and T. M. Mitchell

AFFILIATIONS

Department of Earth Sciences, University College London, Gower Place, London WC1E 6BT, United Kingdom

[a]Author to whom correspondence should be addressed: c.harbord@ucl.ac.uk

ABSTRACT

A new setup to measure acoustic wave velocities through deforming rock samples at high pressures (up to 1000 MPa), temperatures (up to 700 °C), and differential stresses (up to 1500 MPa) has been developed in a recently refurbished gas medium triaxial deformation apparatus. The conditions span a wide range of geological environments and allow us to accurately measure differential stress and strains at conditions that are typically only accessible in solid medium apparatus. Calibrations of our newly constructed internal furnace up to 1000 MPa confining pressure and temperatures of up to 400 °C demonstrate that the hot zone is displaced downward with increasing confining pressure, resulting in temperature gradients that are minimized by adequately adjusting the sample position. Ultrasonic velocity measurements are conducted in the direction of compression by the pulse-transmission method. Arrival times are corrected for delays resulting from the geometry of the sample assembly, and high-precision relative measurements are obtained by cross correlation. Delays for waves reflected at the interface between the loading piston and sample are nearly linearly dependent on differential applied load due to the load dependence of interface stiffness. Measurements of such delays can be used to infer sample load internally. We illustrate the working of the apparatus by conducting experiments on limestone at 200 MPa confining pressure and room temperature and 400 °C. Ultrasonic data clearly show that deformation is dominated by microcracking at low temperature and by intracrystalline plasticity at high temperature.

I. INTRODUCTION

The study of rock deformation under lithospheric conditions is technically challenging since it requires generating high pressures, temperatures, and differential stresses. To simulate shallow crustal conditions (i.e., less than 20 km), corresponding to confining pressures of up to 400 MPa and temperatures of up to 200 °C, triaxial oil medium apparatus are used. They can accommodate large samples (20–100 mm in diameter) and are also typically furnished with pore fluid pressure systems (up to 200 MPa) to allow independent control of confining and pore pressures. Due to their ease of operation, oil-medium triaxial systems are the most widely used apparatus in rock deformation, although they are generally limited to investigations of brittle rock failure only.

More extreme conditions (i.e., greater than pressures of 400 MPa, temperatures of 200 °C, and differential stresses 500 MPa) require the use of a more specialized deformation apparatus, where

confinement is either provided by a solid medium in a piston–cylinder configuration (e.g., Griggs, 1967, and Fig. 1), or an inert gas in a triaxial configuration (e.g., Paterson, 1970, and Fig. 1). Commonly used "Griggs" solid medium apparatus can deform rock samples, up to confining pressures of 3500 MPa, differential stresses of 3000 MPa, and temperatures of 1500 °C, representative of the middle crust to the upper mantle (i.e., up to 150 km burial depth, Fig. 1). "Paterson" apparatus are the most commonly used gas medium triaxial deformation systems and are currently used up to confining pressures of 500 MPa, temperatures of 1500 °C, and differential stresses of 1000 MPa (Fig. 1). In the past, gas apparatus have been used up to confining pressures of 1000 MPa (Heard, 1960; Paterson, 1970). However, a pressure vessel failure at 500 MPa led Paterson to restrict routine confining pressure conditions to 300 MPa (Paterson, 1970).

"Griggs" and "Paterson" apparatus are used to study different deformation regimes. Rock samples deformed in a "Griggs"
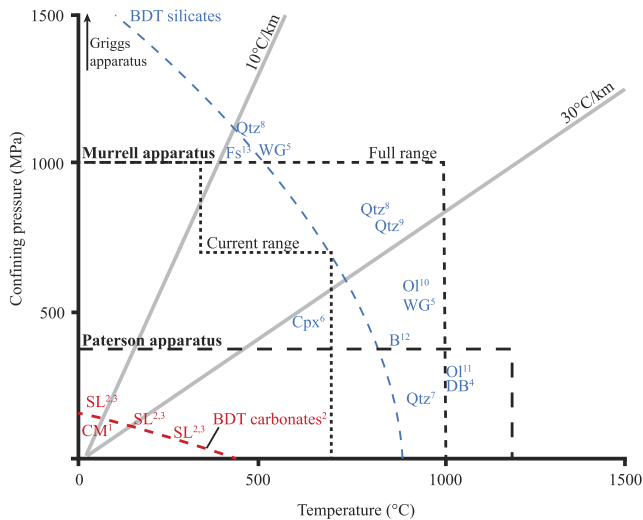
FIG. 1. Design and current operating range of the Murrell triaxial apparatus compared to the approximate onset of the "dry" brittle–ductile transition in rocks (BDT in the figure), modified after Murrell (1990). The range of Paterson apparatus is also shown for comparison (Paterson, 1970), and we also note that the displayed range of conditions can be easily achieved using Griggs' apparatus (Griggs, 1967). CM: Carrara marble [(1). Fredrich, Evans, and Wong, 1989], SL: Solnhofen limestone [(2). Heard, 1960, (3). Rutter, 1974], DB: Maryland diabase [(4). Caristan, 1982], Cpx: Clinopyroxenite [(6). Kirby and Kronenberg, 1984], Qtz: Quartzite [(7). Kanaya and Hirth, 2018, (8). Hirth and Tullis, 1994, (9). Heard and Carter, 1968], Ol: olivine [(10). Raleigh, 1968, (11). Chopra and Paterson, 1981], B: basalt [(12). Violay et al., 2012], and Fs: feldspar (Tullis and Yund, 1992]. The gray lines show typical geothermal gradients of subduction zones (10 °C/km) and mountain belts (30 °C/km), where rocks are actively deformed in the earth's lithosphere.

measure *in situ* physical properties during deformation. *In situ* measurements are easiest in oil medium triaxial apparatus, where large sample dimensions permit the use of a wide range of sensors. At more extreme test conditions, measurements of physical properties are significantly more difficult to obtain. Due to the limited sample size and access, Griggs apparatus are the most challenging apparatus to instrument, and studies have been limited to acoustic emission (Blacic and Hagman, 1977; Ghaffari and Pec, 2020) and axial P-wave velocity (Moarefvand et al., 2021). In gas apparatus, *in situ* measurements during deformation have included volume changes (Fischer and Paterson, 1989), permeability (Fischer, 1992), acoustic emission (Burlini et al., 2007), electrical conductivity (Ferri et al., 2009), and high frequency displacement (Hayward et al., 2016). Other *in situ* measurements at hydrostatic conditions in gas-apparatus include ultrasonic wavespeeds (e.g., Christensen, 1979) and torsional attenuation (e.g., Jackson et al., 1984).

Here, we document modifications that we have made to a recently refurbished high pressure vessel, the "Murrell" [after Professor Stanley Murrell, 1929–2004, see Edmond and Murrell, 1973; Ismail, 1974; Jones, 1989; Murrell et al., 1989]. The apparatus is capable of deforming rock up to confining pressures of 1000 MPa, temperatures of 1000 °C, and differential stresses of 1500 MPa. First, we describe the mechanical and electrical components of our gas apparatus. Results from calibration of our internal furnace at a range of confining pressures (200–1000 MPa) and temperatures (100–400 °C) are reported. Following this, we document our recently commissioned ultrasonic velocity measurement system. We demonstrate how this new acoustic data can be used to obtain information about deformation mechanisms during experiments using limestone at room temperature and 400 °C. We find that a non-negligible transmitted wave delay occurs as a result of interfacial compliance and suggest appropriate correction methods. We also show that the delay associated with interfacial compliance can be used to obtain internal load using reflected wave measurements.

II. APPARATUS DESCRIPTION

A. Pressure vessel

The pressure vessel, of a composite construction, is made of vacuum forge remelted Hecla tool steel (Fig. 2). The vessel has a maximum design confining pressure of 1400 MPa, a working confining pressure of 1000 MPa, and a maximum working temperature of 1000 °C using inert gas as a confining medium. Hecla 180 alloy (Table I) is used for the vessel body (Fig. 2) with a tensile strength of 1240 MPa (OD 635 mm, ID = 220.05 mm) and is lined with Hecla 174 (Fig. 2 and Table I) with a tensile strength of 1420 MPa (220.95 mm OD, 80 mm ID). The liner was inserted into the external vessel using shrink fitting. An interference fit between the external vessel and liner results in static compressive hoop stress at the outer radius of the liner. This equates to ≈400 MPa at the internal diameter of the vessel liner, and thus, tangential stress in the vessel only becomes tensile when the internal confining pressure exceeds 400 MPa.

B. Axial piston and top plug

Load is applied to samples through the top plug using a piston with a double step in diameter to provide compensation for the

apparatus are relatively small (6.3 mm in diameter and 12 mm in length). Axial load and confining load are measured externally, which results in inaccuracies in the determination of the internal stress state (Holyoke and Kronenberg, 2010). Therefore, solid medium apparatus are suited to deforming materials in high stress regimes, and careful calibrations are required to obtain reliable strength measurements (e.g., Gleason and Tullis, 1995; Holyoke and Kronenberg, 2010). In a "Paterson" apparatus, samples are larger (10–15 mm in diameter and about 20 mm in length) and differential stress is measured internally. These factors result in considerably better accuracy in measuring differential stress and strain, making the gas apparatus ideal to study material deformation in the high temperature, low stress regimes. However, their limited differential stress capacity (up to 1000 MPa) makes them less suitable for work on low temperature plasticity. Recent work by Burdette, Kidder, and Hirth (2021) has started to bridge the gap between the traditional capabilities of solid medium "Griggs" and gas medium "Paterson" apparatus by significantly improving load resolution measurements in a modified "Griggs" system equipped with a laser interferometer.

Generally, rock deformation experiments are complemented by post-mortem microstructural investigations. As a result of unloading, decompression, and cooling, post-mortem microstructural investigations are prone to artifacts, and it is, therefore, desirable to
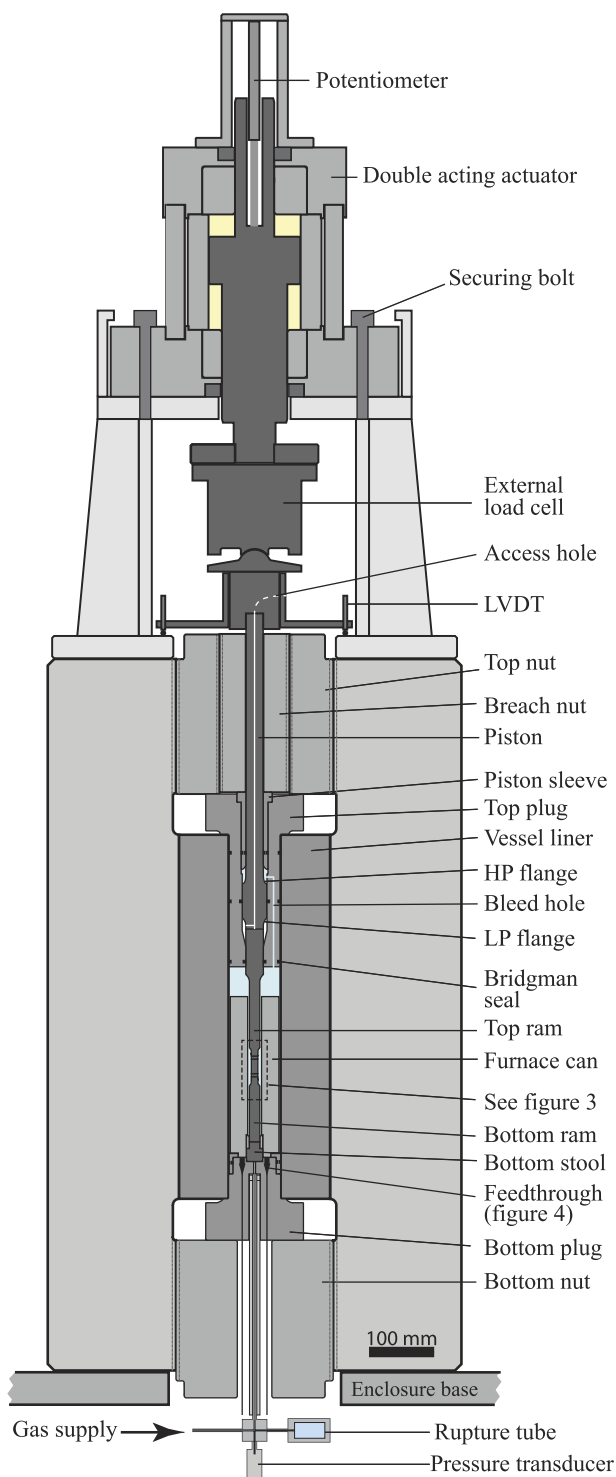
FIG. 2. Annotated scale sectional view of the Murrell deformation apparatus. Light blue shading indicates the location of the confining argon gas, and yellow shading indicates the location of hydraulic oil. LP flange is low pressure flange, and HP flange refers to the high pressure flange. Further details of sealing arrangement are shown in Fig. 3, sample assembly in Fig. 4, and feedthroughs in Fig. 5.

effect of confining pressure (Fig. 2). The piston is made from D6 tool steel (58–60 Rc), with a length of 489 mm, a rod diameter of 27 mm, and a piston section of 38 mm in diameter. The piston section is flanged into the rod with two shoulder fillets. The upper flange (HP flange, Fig. 2) is elliptical in profile and forms part of the high pressure section of the compensation system and is in a tensile stress condition. The lower flange (LP flange, Fig. 2) is circular in profile and forms part of the low pressure compensation chamber and is subjected to compressive loads. The upper flange of the piston was originally designed with a shoulder fillet of circular section; however, after several catastrophic tensile failures of the piston, it was changed to an elliptical section (Jones, 1989), due to its favorable reduction of stress concentrations (Peterson, 1974). The piston has a central bore of 4 mm diameter, allowing access for pore fluid or a range of sensors. Its base is machined with an M12 thread to allow interchange of the rams.

Sealing of the piston and pressure autocompensation is achieved using six sets of annular Bridgman seals (Bridgman, 1914; Griggs, 1936; Holloway, 1971; Tullis and Tullis, 1986, Fig. 3), which are combined with a network of bores to distribute or vent the confining gas. Bridgman seals in this configuration follow the descriptions of Griggs (1936) and comprise a stack of 3 mitre rings (two phosphor bronze and a single mild steel ring), which are chamfered at 30° and sandwich a single nitrile O-ring (Fig. 3). Pressure is transmitted onto the mitre rings and O-ring using a hardened D2 steel plunger (58–60 Rc), which is supported by the seal housing. The seal arrangement is symmetric about a fin extending from the seal support backing and between the external and internal seal stack. Nitrile O-rings with a shore hardness of 70 are used, which swell due to their high argon solubility. To reduce seal friction, seals are also lubricated with Molykote 55 O-ring grease, which also aids the swelling of the O-ring material. The current sealing arrangement has been used up to a confining pressure of 1000 MPa without leakage, although considerable wear and damage is observed when using the seals above 600 MPa confining pressure.

C. Sample assembly

The sample assembly comprises a top and bottom ram, two sample spacers, two swaging rings, an annealed copper jacket, and a rock sample (Fig. 4). The top ram attaches to the base of the piston using an M12 stud, and the upper portion of the top ram forms a high pressure sealing surface with the lowermost Bridgman seals in the top plug (Fig. 2). Ram diameter is reduced using 3 large radius blends to the final 10 mm sample diameter. Sealing of the jacket is achieved by swaging tapered steel or nickel alloy rings over the ends of the jacket and the rams, where ram diameter increases from 10 to 10.4 mm, similarly to the technique used by Handin (1953) and Heard (1960) (see Fig. 4). To avoid stretching and work hardening of the jacket during swaging, which can cause jacket puncture, light polish and a small quantity of MoS_2 grease are applied to the jacket surface before swaging.

A range of ram configurations is used depending on the experimental requirements. For temperatures less than 200 °C, rams are fabricated from D2 tool steel (58–60 Rc), which can be used up to the maximum working pressure of the vessel, and differential stress of 1500 MPa. For temperatures up to 700 °C, the rams are fabricated from Inconel 718 (36–38 Rc) and can be used up to 1000 MPa

TABLE I. Composition of the two types of steel constituting the pressure vessel.

	C	Si	S	P	Mn	Cr	Ni	Mo	V	Fe
Hecla 180	0.40	0.27	0.012	0.016	0.70	1.22	3.10	0.46	0.16	bal.
Hecla 174	0.42	1.18	0.010	0.016	0.34	5.12	⋯	1.30	0.95	bal.

differential stress and 630 MPa confining pressure. In order to provide access for pore fluids or thermocouples, a hollow top ram can be used. In principle, other modifications are possible to extend the range of conditions or to integrate an internal load cell.

D. Bottom plug, bottom stool, and feedthroughs

The bottom plug forms the lower closure of the pressure vessel and is fabricated from 50 Rc Hecla 174 steel (Table I). A single annular Bridgman seal is used to seal the external diameter of the bottom plug (Fig. 2). The bottom plug is equipped with 12 Bridgman type feed through connections (Bridgman, 1914). There are three 7 mm diameter high current power feedthroughs [Fig. 5(a)] and nine 5 mm diameter electrical feedthroughs [Fig. 5(b)]. Each feed through hole is machined with a 20° conical section, which forms the sealing surface against the feedthrough cores. Feedthroughs are isolated from the bottom plug using Vespel sheaths on the 20° sealing surface and Carp brand Tufnol on the high pressure side. Historically, pyrophyllite was used to isolate feedthroughs, but it was found to be unreliable due to its poor machinability, high porosity, and brittleness after fabrication. PEEK plastic was also recently trialed; however it crept severely, shorting the feedthrough connection.

The nine smaller holes are used for electrical connections (thermocouples or to pulse a piezoceramic) and comprise a 420 stainless steel cone with two 1.2 mm diameter blind holes [Fig. 5(b)]. A short section of tinned copper wire is brazed into either end of the cones, six of which are connected to a chromel or alumel wire, acting as leads for K-type thermocouples. The remaining three small

feedthroughs can be used for a variety of purposes. The three larger 7 mm diameter 420 stainless steel cones are used to supply power to the furnace. The cones are constructed with two blind holes into which a section of the copper rod is brazed in place. Each feedthrough wire is terminated inside a copper banana jack that fits into the base receptacle of the furnace.

Argon gas is supplied to the vessel through a central bore drilled along the axis of the bottom plug, entering the vessel at the base of the bottom stool [Fig. 2(a)]. The bottom stool acts as a receptacle for the bottom ram and rests in a 6 × 25 mm diameter recess machined into the center of the bottom plug [Fig. 7(b)]. A tapered ring attached to the bottom stool acts as a centering guide for the sample assembly that is inserted from above.

E. Pressure generation and decompression

Gas is compressed and decompressed using a computer controlled four-stage hydraulically driven gas intensification system manufactured by Sovereign Pressure Products, Ltd., UK. Control and monitoring of the system are performed by use of a human–machine interface or a LabView program. Before pressurization, it is standard practice to perform two purge cycles to flush the system of atmospheric air. A pressure of 600 MPa can be reached within 10–20 min, although pressurization is performed in stages over a
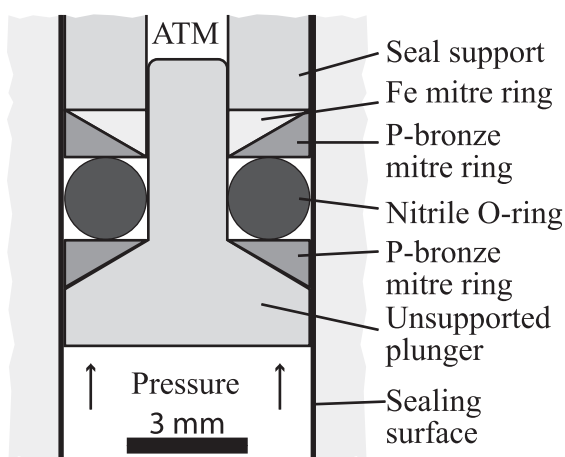

FIG. 3. Detailed sectional scale sketch of annular Bridgman seals following Griggs (1936) and Holloway (1971). Fe = mild steel and P-bronze = phosphor bronze. See text for a full description of the sealing configuration.
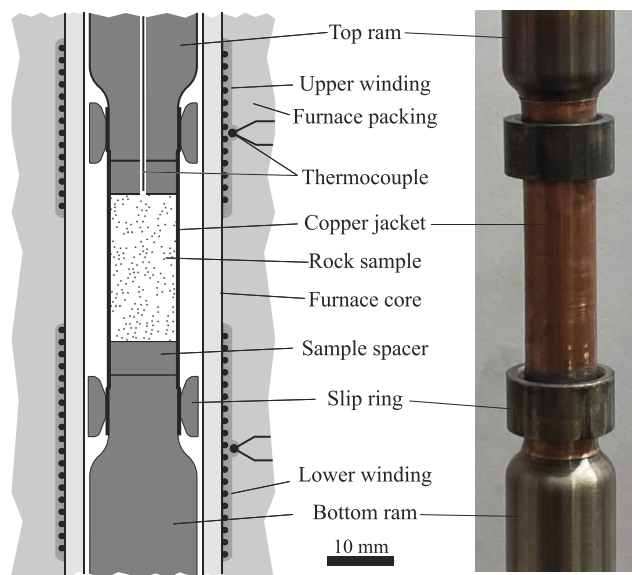

FIG. 4. Scale section view of sample assembly and furnace core, showing the key components of the configuration, supplemented by a picture of the sample assembly before insertion into the apparatus.
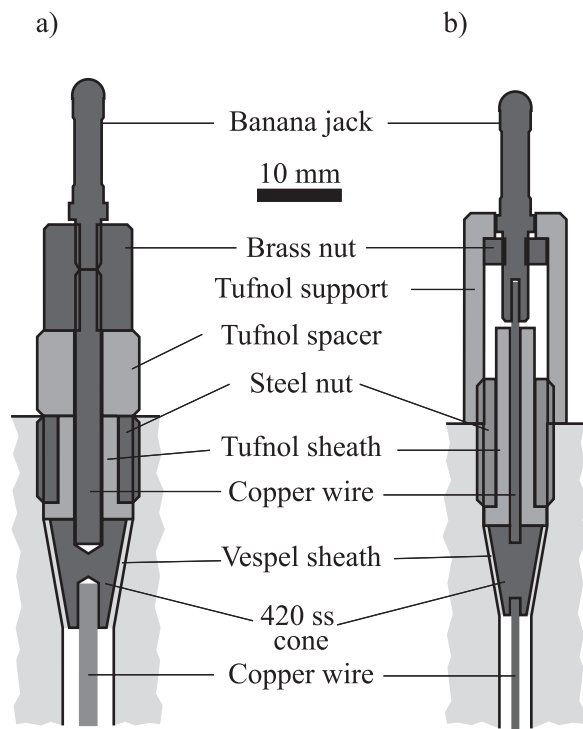
FIG. 5. Detailed sectional scale sketch of feedthroughs in the bottom plug. Inset (a) shows power feedthrough, which is of large diameter for high currents. Inset (b) shows smaller diameter feedthrough used for electrical connections.

period of an hour to limit sample damage. Decompression is also computer controlled using a sequence of hydraulically and pneumatically actuated flow restrictors. It is also performed in several steps to avoid sample damage and limit condensation of water vapor along pipe fittings.

F. Actuator, load, and displacement measurements

A double acting servo hydraulic actuator attached to the top of the pressure vessel can apply loads of up to 200 kN (i.e., differential stress of 2550 MPa on a 10 mm diameter sample). The back of the actuator is fitted with a large range potentiometer, which is used for coarse control of the actuator when not in contact with the piston. Load from the actuator is transmitted through a 20 tonne load cell (Eliott brothers, SC-50000) onto a hemispherical seat and a head block (Fig. 2). Fine displacement is measured using two removable linear variable differential transformers (LVDT) attached to the head block (RDP, model GT5000-L25, LVDT Fig. 2), which are used to control displacement during sample loading.

G. Furnace assembly and calibration

The internal furnace is housed in a stainless steel sleeve (80 mm OD, 74 mm ID, 230 mm length) and follows the design of previous workers (Paterson, 1970; Holloway, 1971; Paterson, 1990). Two windings of Kanthal A1 wire (Al5.8Cr22Fe72.2) are positioned along the alumina furnace core (outer diameter of 23.4 mm, the inner

diameter of 17.4 mm, and 126 mm in length) and are wired in series (Fig. 4). Windings are potted and affixed to the core using glass cement (Glassbond Sauereisen 78/3), and the core is held in place using Macor ceramic spacers. The remaining volume between the core and the can is packed using a combination of alumina paper (Zircar ceramics APA 2) and fiber (Zircar ceramics Alumina Bulk Fiber). Basal female banana jack receptacles, used for electrical connections, are held in place using a Carp brand Tufnol plate, with either end of the internal assembly secured using two brass plates.

Two K-type thermocouples are used to monitor the upper and lower winding temperature and are vertically centered with respect to the individual windings. A third "safety" thermocouple is positioned next to the stainless steel sleeve to monitor the vessel wall temperature. In order to avoid retempering the vessel liner steel by applying excessive temperatures, the furnace power is cut if the temperature measured by the safety thermocouple exceeds 400 °C. All three thermocouple temperatures are monitored using a Eurotherm NanoDac controller. Power to the windings is controlled using two Eurotherm Epack 1 PH digital silicon controlled rectifiers wired in series with two step down transformers. Both the NanoDac and E-pack units are controlled and logged using LabView and are calibrated for use with constant power.

The power input to the furnace coils must be calibrated to produce target temperatures at the sample location at a range of pressure conditions. The calibration was performed by measuring temperature profiles across the sample location using a K-type thermocouple inserted in a hollow alumina sample. The thermocouple was attached to a miniature linear actuator (model: Actuonix L16P), with position measured using feedback from an onboard potentiometer. The actuator is controlled from LabView using the libraries provided by Actuonix (https://www.actuonix.com/category-s/1930.htm), and profiling is repeated three times at each calibration condition (see Fig. 6).

Calibrations have been performed at 200 MPa intervals in confining pressure up to 1000 MPa and at 100 °C temperature intervals up to 400 °C. During the calibration, the thermocouple position was stepped at 2–3 mm intervals in the range of 0–60 mm above the top of the bottom stool (see Figs. 4 and 6). The position of the thermocouple was held at each position for at least 30 s to capture temporal variations in temperature and allow the thermocouple tip to equilibrate with the ambient temperature. The scatter at each point on the calibration plot reflects temperature fluctuations during hold periods, likely resulting from argon convection (Fig. 6).

Temperature profiles demonstrate that the elevation of the hot zone decreases with increasing pressure [contrast Figs. 6(a) and 6(e)]. We obtain temperatures within about 10 °C of the mean in the 150–200 °C range and 15 °C in the 300–40 °C range. Increases in pressure tend to improve the temperature profile. Paterson (1970) previously observed a downward displacement of the hot zone with increasing pressure, which can be explained by the increased density of argon at high pressure. The temperature dependence of argon density is lower at higher pressure (Gosman, McCarty, and Hust, 1969) and, therefore, the buoyancy potential that drives convection is smaller. As a result, convective heat loss is suppressed, resulting in a downward displacement of the hot zone. Based on the observed change in hot-zone elevation, we introduced an extended bottom ram, with 15 mm extra length to position samples more favorably for lower pressure experiments.
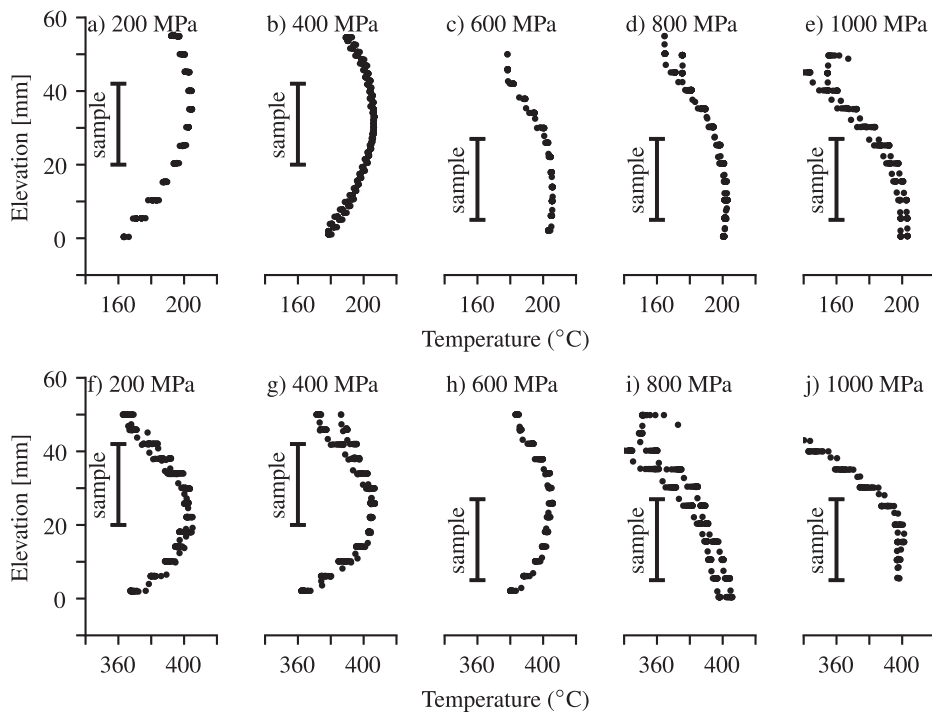
FIG. 6. Calibration of the internal furnace at a range of confining pressures and temperatures, elevation is in mm and is relative to the top of the bottom ram. Insets (a) to (e) show calibrations at a target temperature of 200 °C and 200 MPa confining pressure intervals up to 1000 MPa. Insets (f) to (j) show calibrations at a target temperature of 400 °C and the same pressures as the 200 °C calibrations. The vertical bars show the positions where rock samples are used at each calibration condition.

H. Safety

In order to reduce the risk posed by a catastrophic gas leak, several safety measures are employed. The entire vessel and pressure generation system are enclosed in an interlocked steel cage (25 mm in thickness), which is lined with wood to absorb projectile energy. The base of the enclosure is made from thin plate steel, with the bottom plug exposed to the ground, which would direct any blast energy downward. Bolts are used to secure individual enclosure components together, with slots machined in the support structure to allow the enclosure to rise during a catastrophic failure. Full rig operation can be performed remotely; however, when the user is working in the laboratory, ear defenders are worn at all times. The vessel and seals are typically checked every 3 months for signs of significant wear or corrosion, and the bottom plug and nut are removed on an annual basis to perform a full vessel inspection. To prevent the vessel and fittings from being overpressured, an 1120 MPa rated rupture tube is installed at the base of the apparatus (Fig. 2).

I. Data reduction

Raw mechanical data must be corrected in order to obtain the true stress–strain response. The absolute value of top plug seal friction is subtracted from load cell measurements before sample contact is made. The seal friction is typically around 4.5 kN at 200 MPa, increasing to around 45 kN at 800 MPa, is not sensitive to internal temperature, and is stable with displacement (see the supplementary material). As seal friction is dependent on confining pressure, an additional correction for seal friction is applied to the data after the hitpoint to account for changes in confining pressure.

A further contribution for the fraction of load supported by the copper jacket is computed from the creep equation of copper given by Frost and Ashby (1982). We do not take into account the strain hardening of the jacket material. Load point displacement is corrected for the loading stiffness that contributes to the recorded LVDT displacement. Loading stiffness obtained by deformation of a steel blank was determined to be 68.9 kN mm^{-1} for the D2 sample assembly and 65 kN mm^{-1} for the Inconel 718 sample assembly.

III. ULTRASONIC VELOCITY MEASUREMENTS

A. Sensor array

Our acoustic array consists of two Lead Zirconium Titanate ceramic (PZT-5H) transducers, positioned outside the hot zone, and within the top and bottom ram, respectively (Fig. 7). The top ram sensor is a commercially made acoustic transducer (Olympus M1106, central frequency 4.7 MHz) and is positioned against a flat recessed section at the end of the M12 threaded section within the top ram [Fig. 7(a)]. A modified stud connector is used to spring load the transducer and align it with the ram axis. The bottom ram sensor consists of a PZT plate positioned into a 4 mm deep, 9 mm diameter recess at the base of the bottom ram, bonded using silver loaded epoxy [Fig. 7(b)]. The bottom of the transducer contacts a spring-loaded copper electrode housed within the bottom stool that is connected to a feedthrough wire. This arrangement of transducers results in easy maintenance of the system, allowing us to swap or remove transducers without removing the upper and lower closure nuts. Both transducers are pulsed and monitored using a Eurosonic USB8M pulse-receiver unit [Fig. 7(c)]. Although the current system

a) top ram piezo mount (TR-pzt)

b) bottom ram piezo mount (BR-pzt)

c) array schematic
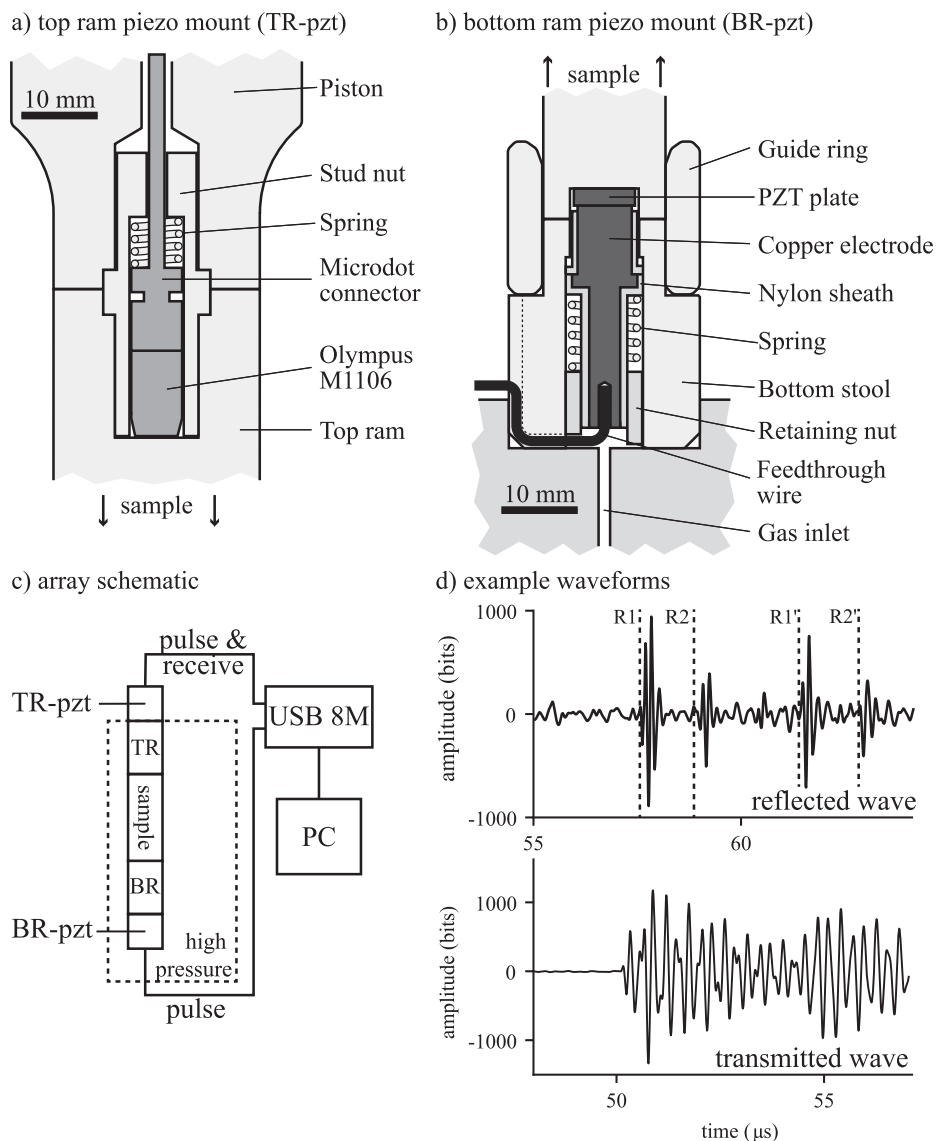
d) example waveforms

FIG. 7. Detail of piezoelectric ceramic placement in (a) the top ram, within a modified stud nut, and (b) glued into a recess at the base of the bottom ram. A spring loaded electrode mounted within a modified bottom stool is used to provide excitation to the bottom ram transducer. Inset (c) shows a schematic illustration of the Lead Zirconium Titanate (PZT) array used to measure acoustic velocity. Inset (d) shows examples of reflected and transmitted waveforms received by the top ram transducer. R1 is the reflection from the interface between the top ram and the sample spacer, and R1′ is the focus of internal reflections generated by R1. R2 is the reflection from the interface between the sample spacer and the sample, and R2′ corresponds to the focus of internal reflections generated by R2.

is set up to make active measurements, a separate oscilloscope could be setup to record passive signals.

B. Transmitted wave measurements

Wave speed in the sample is measured using the pulse-transmission method (Birch, 1960). To do this, the bottom ram PZT transducer is excited by a 2.5 MHz, 200 V pulse, which is received by the sensor positioned within the top ram [Fig. 7(c)]. The receiving sensor is pre-amplified at 40 dB and recorded at 100 MHz with 12 bit accuracy, and signal quality is improved by stacking 256 individual measurements at each time interval. In this configuration, the velocity can be measured every 0.5 s.

During experiments, relative changes in arrival times are computed by cross correlation of individual waveforms against a manually picked "master" waveform. In order to increase the arrival time accuracy, the raw waveforms are sub-sampled at 10 times the original sampling frequency using cubic interpolation. Following re-sampling, the signals are cut with a window centered around the arrival time. The arrival time is then computed by cross correlating the trimmed signals, with the offset time, δt, taken as the time difference corresponding to the maxima of the correlation function between the master and test waveform.

The travel time through the sample is calculated by removing the delay resulting from the sample assembly. Time delay through the loading column changes with load, pressure, and temperature; the column shortens elastically as a result of load and pressure, but it can also expand thermally. To measure delays resulting from the sample assembly, we performed a series of calibration runs using a flawlessly fused silica blank, which has a known wave velocity

that does not vary significantly with pressure. We cycled load on the sample at 200 and 400 MPa confining pressure and also performed a cycle at a temperature of 200 °C.

When removing all possible contributions related to the changes in sample and loading piston length, we still observe a small time delay (0–20 ns) that varies with load (Fig. 8). This delay is interpreted to arise from changes in the contact compliance of loaded interfaces (Pyrak-Nolte *et al.*, 1987; Möllhoff and Bean, 2009). Interface group time delay is directly proportional to contact compliance (Pyrak-Nolte *et al.*, 1987). Contact compliance is also known to decrease with increasing load (Greenwood and Williamson, 1967; Pohrt and Popov, 2012); therefore, the remaining time residual is interpreted to result from these changes. Greenwood *et al.* (1967) predict that compliance is approximately proportional to the ratio of root mean square of surface elevation to the normal force. All contacting surfaces are ground using a 5 μm diamond wheel to ensure parallelity prior to tests. Therefore, at low compliance interfaces, such as the nominally flat ground metal and rock surfaces used here, the change in arrival time is expected to be linear with load (Pyrak-Nolte *et al.*, 1987). In calibrations with a fused silica blank, the remaining interface time delay demonstrates a reasonable degree of linearity up to 30 kN load at all test conditions (Fig. 8).

Since interface time delay depends on the composite elastic properties of contacting interface (Schoenberg, 1980), the time delay will also vary with the sample used. Therefore, we need to correct each experiment on an individual basis. To do so, we first correct δt for the load column and sample shortening. Then, we fit the initial change in δt vs differential load immediately following the "hit-point" between 1 and 4 kN. At such low loads, any cracking in the sample will be preferentially aligned parallel with the sample axis; therefore, axial P-wave speed is expected to remain nearly constant and changes in arrival time will be dominated by changes to the interface time delay. The obtained linear fit of δt vs load is then used to correct δt as a function of load during the entire experiment.

To test our system, we deformed two samples of the Solnhofen limestone at 20 and 400 °C, at a strain rate of 1×10^{-5} s^{-1}, and a confining pressure of 200 MPa. At low strain, differential stress increases linearly with strain, corresponding to elastic loading of the sample [Figs. 9(a) and 9(b)]. After the initial elastic loading, the differential stress rolls over with strain corresponding to yield of the sample. Differential stress continues to increase after yield during the entire experiment and indicates strain hardening behavior. Yield stress

and final differential stress levels are higher in the room temperature experiment [Fig. 9(a)], in comparison with the experiment at 400 °C [Fig. 9(b)].

The differences in mechanical data are also reflected in the measured arrival times [Figs. 9(c) and 9(d)] and subsequent velocity computation [Figs. 9(e) and 9(f)]. Both picked arrival times show a reduction in travel time during initial loading [Figs. 9(c) and 9(d)], largely as a consequence of interface compliance changes and elastic shortening of the sample. Following the initial decrease in arrival time, at 20 °C, the arrival time increases slightly before remaining relatively constant [Fig. 9(c)]. In the 400 °C experiment, the arrival time continues to decrease at a smaller rate than the initial decrease [Fig. 9(d)].

To test the correction, velocity was in calculated two ways: first, by removing the known, load dependent travel time through the sample assembly [Figs. 9(e) and 9(f), "uncorrected" black curve] and, then, by removing the estimated interfacial time delay [Figs. 9(b) and 9(d), "corrected" gray curve], based on the arrival time changes during initial loading of the sample (differential load of 1–4 kN). Velocity is simply the ratio of sample length to travel time and is normalized by the initial velocity at the experiment hit point. The corrected sample P wave velocity drops considerably after initial elastic loading at 20 °C [Fig. 9(e)] but remains relatively constant at 400 °C [Fig. 9(f)]. The correction removes the large increase in velocity during the initial elastic loading of the sample [Figs. 9(e) and 9(f) gray curves]. However, the correction procedure maintains quantitative differences between individual experiments and does not significantly affect relative changes after yield.

Changes in P wave speed can be used to infer the microstructural state of the sample. Velocity reduces when tensile microcracks propagate in the sample. At 20 °C, the large decrease in wavespeed suggests that cracking is the dominant deformation mechanism [Fig. 9(e)], which is consistent with the observation of Baud, Schubnel, and Wong (2000). At 400 °C, however, the relatively small decrease in wavespeed results from the increased activity of plastic deformation mechanisms that are expected at these conditions (Heard, 1960). Plastic deformation suppresses crack growth, which can explain the small decreases in wavespeed.

The key advantage of having access to wave velocity *in situ* is clear when comparing the relatively minor differences in stress–strain behavior between the tests conducted at 20 and 400 °C [Figs. 9(a) and 9(b)] to the large qualitative difference in wave velocity evolution [Figs. 9(e) and 9(f)]. Stress–strain behavior cannot be used here to distinguish between microscale
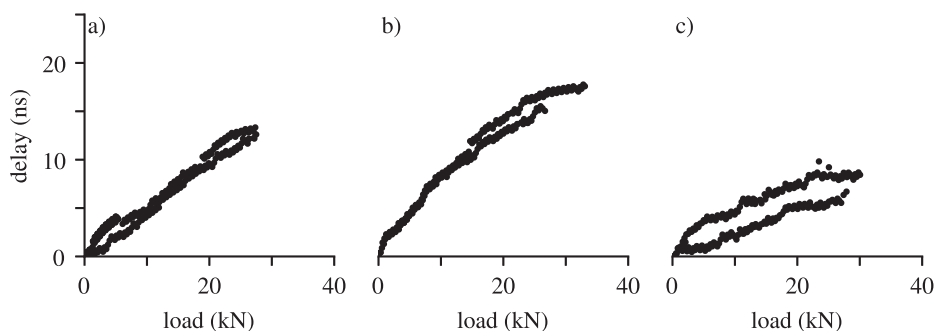

FIG. 8. Time residual after removing contributions to time delay resulting from an elastic shortening of the load column at a range of test conditions. Insets: (a) 200 MPa at room temperature, (b) 200 MPa at 20 °C, and (c) 400 MPa at room temperature.
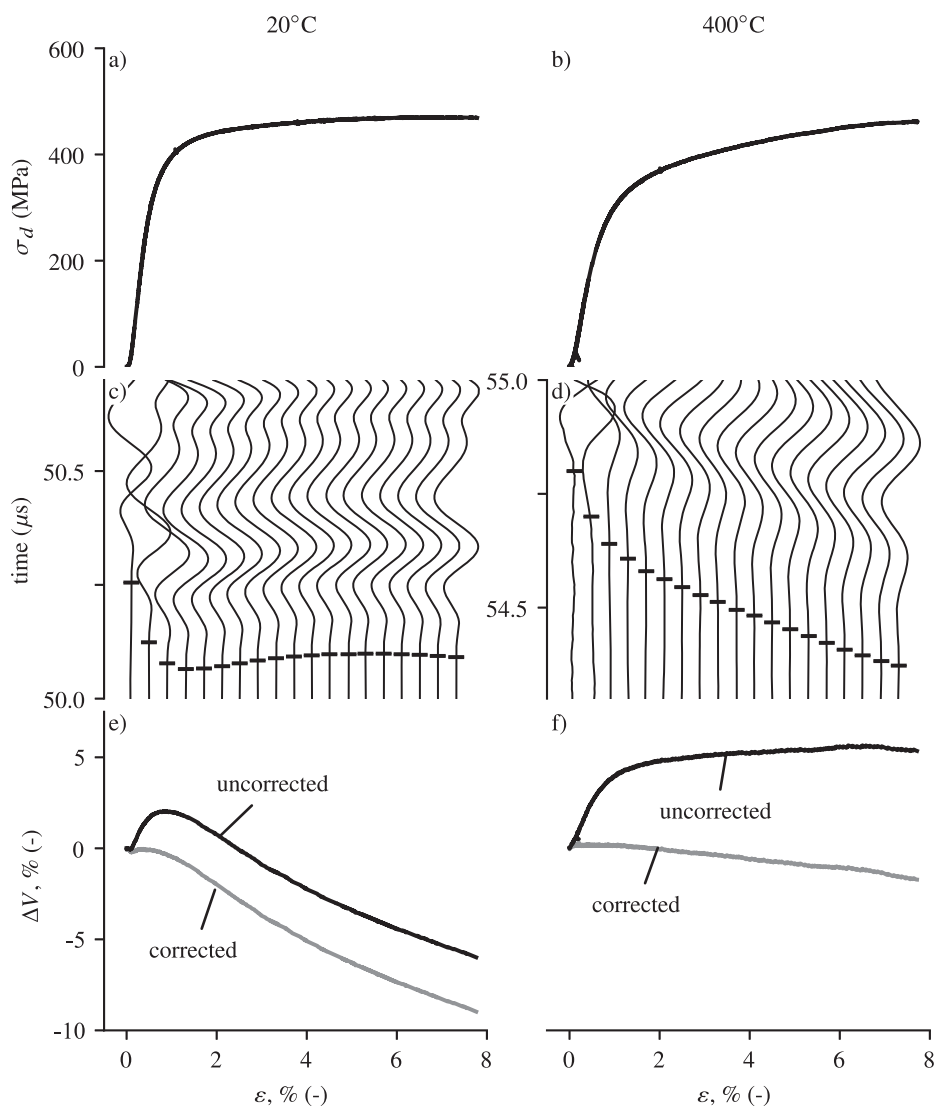
FIG. 9. Examples of mechanical data and transmitted wave measurements during the deformation of Solnhofen limestone samples at 20 and 400 °C and 200 MPa confining pressure. Inset (a) is the stress–strain curve obtained at 20 °C and (b) the stress–strain curve at 400 °C. Insets (c) and (d) show example raw transmitted first arrival waveforms received at the top transducer normalized by the maximum possible value (=2048 bits), and the horizontal bars indicate the arrival time obtained using cross correlation. Insets (e) and (f) show the computed compressional wave velocity changes. The uncorrected data (black curve) are calculated without any correction for interfacial load delay, and the corrected data (gray curve) show the effects of using the interfacial load delay correction.

deformation processes, and careful microstructural work on post-mortem samples would be needed to establish those, with caveats due to potential damage and cracking during quenching and decompression. *In situ* wave velocity measurements largely circumvent those issues, at least to identify regimes where microcracking dominates.

C. Reflected wave delay as a piezometer

The most accurate and reliable measurements of stress on samples in a pressure vessel are obtained from an internal load cell located within the high pressure chamber where seal friction does not contribute to the load. Interfacial reflected wave time delay is also sensitive to changes in interface compliance (Schoenberg, 1980; Pyrak-Nolte, Cook, and Myer, 1987) and could, therefore, be used to measure load internally. Here, we present a new technique to obtain

load using interfacial group delay, which allows differential stress to be measured accurately without needing to correct for seal friction.

In order to test reflected wave delay as a proxy for differential stress, we recorded reflected waves during load cycles with a fused silica blank (Fig. 10). The 10 mm diameter silica sample was load cycled at 20 and 200 °C at 200 MPa confining pressure and also at 20 °C at 400 MPa. We then used the second reflected arrival [R2, see Fig. 7(d)], corresponding to the sample spacer–sample interface, and used cross correlation to obtain the change in arrival time [Figs. 7(a) and 7(c)]. In these load cycles, a delay of ≈4 ns kN^{-1} is typical [Figs. 11(a) and 11(c)], which, when combined with a sub-sampling frequency of 1 GHz, results in a resolution of about 2 MPa differential stress.

We now apply this technique to the previously discussed experiments performed with the Solnhofen limestone, where we also measured reflected wave arrivals during the test. The sample
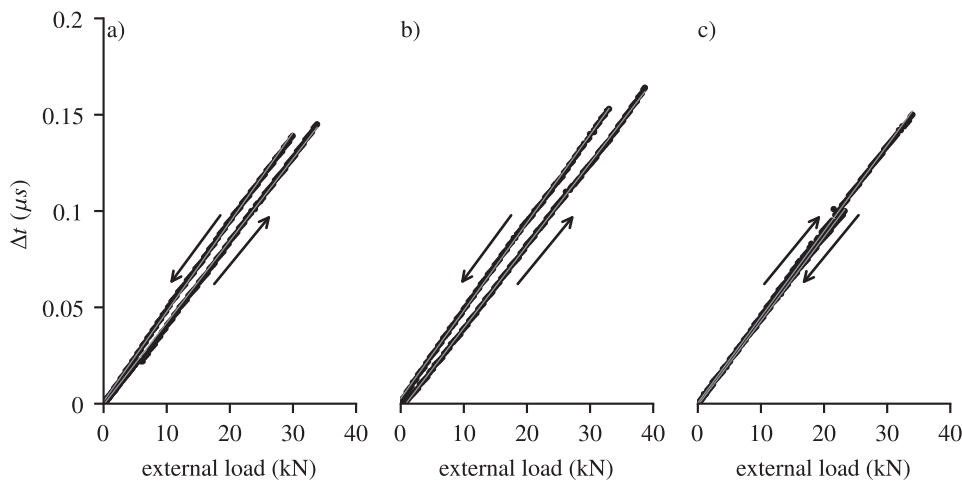
FIG. 10. Top piston reflection delay calibration during load cycles with a fused silica blank at a range conditions with hysteresis due to seal friction removed. Insets: (a) load cycle at 20 °C, 200 MPa confining pressure; (b) 200 °C, 200 MPa confining pressure; and (c) 20 °C, 400 MPa confining pressure. Arrows indicate loading sense, black scatter is the raw data, and the overlaid gray curve is a linear best fit of the data.

spacer–sample interface reflection was used in the cross correlation analysis [R2, Fig. 7(d)]. The calibration was made on an individual basis for each experiment using the measured changes of δt during elastic loading phase of the experiment. Results show that this measurement is able to reproduce the stress measurements accurately at 20 °C [Fig. 11(b)] and reveals extra details during the unloading phase of the experiment. In particular, it provides an accurate measurement of the stress–strain behavior at the onset of unloading and throughout the unloading phase. The inflection in stress–stress

behavior observed at low load [Figs. 11(b) and 11(d)] can provide information about residual stresses stored within the sample (e.g., Hansen et al., 2019). These observations are normally obscured in external load measurements due to hysteresis resulting from the top plug seal friction. At higher temperatures, the large stress changes during initial loading and unloading are well matched. However, during strain hardening, temperature fluctuations lead to variations in the stress computed using this measurement [Fig. 11(d)].
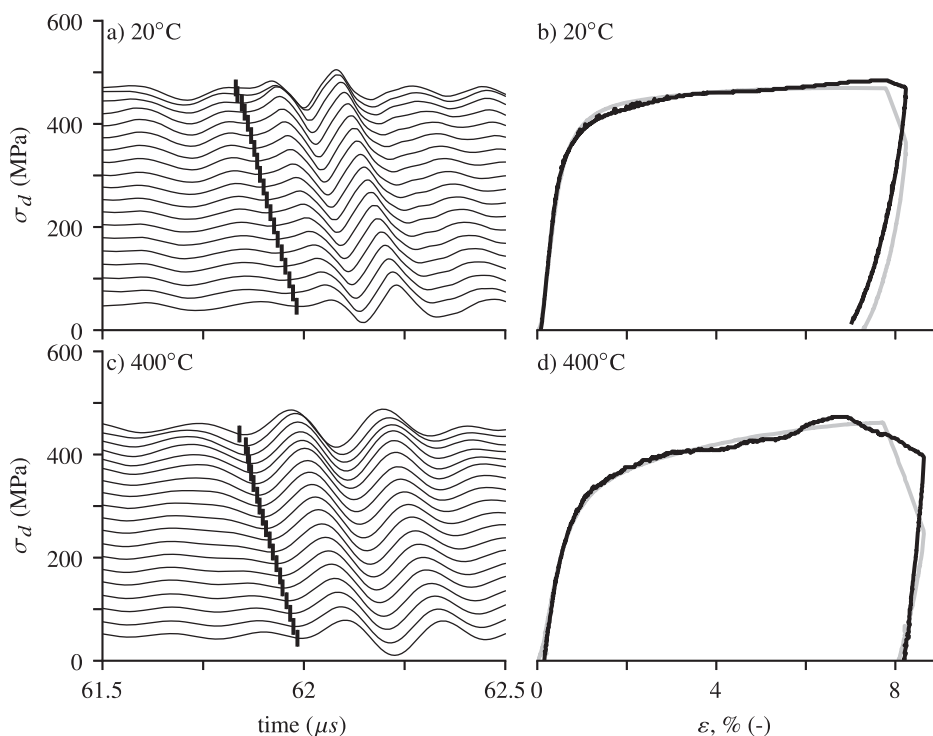

FIG. 11. Top piston reflection delay calibration from experiments conducted with the Solnhofen limestone at 20 and 400 °C and 200 MPa confining pressure. Insets (a) and (b) show raw waveforms obtained during loading of the sample that is used to derive the calibration between load and delay time. Vertical bars indicate arrival times obtained using cross correlation. Insets (c) and (d) show the use of this calibration to obtain stress. The stress–strain curves in gray are the data obtained from the external load cell, and the black curves data are obtained from the reflected wave delay. Fluctuations in stress after yield in the high temperature experiment are a result of temperature changes resulting from argon convection.

Looking to other applications, reflected wave measurements could also be used in stress relaxation experiments where piston motion is arrested. In these tests, the differential stress state is obscured by seal friction, which this technique overcomes. This technique also has potential for use in other apparatus, where space is limited, or it is not possible to position a sensor due to harsh environmental factors. In particular, it may be a useful technique to obtain load in solid medium apparatus that suffer from large uncertainties resulting from seal friction (Holyoke and Kronenberg, 2010). It would also directly complement the method suggested by Moarefvand *et al.* (2021), where arrival times of use transmitted waves are used to infer column length in a Griggs apparatus.

IV. CONCLUSIONS

In this article, we discussed and detailed the modifications, complete refurbishment, and upgrades made to a high-pressure high-temperature gas apparatus in order to bring it back into working service. The apparatus can actively monitor acoustic wavespeed during deformation up to confining pressures of up to 1000 MPa and temperatures of up to 700 °C. We discussed the construction and calibration of an internal furnace, and the effects of varying pressure and temperature on the temperature profile, showing that the hot zone elevation decreases with increasing pressure. In calibrating the acoustic velocity measurements, we observed a load dependent time residual that is not accounted for by elastic shortening of the load column. The load dependent time residual is interpreted to result from changes in interface compliance, which result in an interfacial time delay that must be subtracted from the travel time measurements. The interface delay is material dependent, and we, therefore, present a technique to estimate this on an individual experimental basis and show how it influences results. As this delay is unique function of load, we demonstrate how it can be used to measure load internally, using reflected pulses, which gives a more accurate measurement of sample stress. Our new technique for measuring load could be developed further to measure load accurately in other similarly inaccessible environments, where it is not possible to position a conventional load cell. Our acoustic array could easily be upgraded to make passive measurements of acoustic emission from the sample. S-wave transducers could also be used to measure the shear wave velocity of the sample during deformation.

SUPPLEMENTARY MATERIAL

See the supplementary material for details of the seal friction stability and technical drawings of components discussed in the main text.

ACKNOWLEDGMENTS

We would like to thank John Bowles, Steve Boon, and Neil Hughes for technical support as well as Paul and Mark Freeman of Sovereign pressure products for support with the gas intensification pump. Colin Jones and Phil Meredith provided highly valuable historical records about the apparatus. Experimental techniques were enriched by discussions with Toshi Shimamoto,

Ian Jackson, Kathryn Hayward, Lars Hansen, Greg Hirth, Dave Dobson, Julian Mecklenburgh, Alexandre Schubnel, Marie Violay and Peter Sammonds. Reviews from two anonymous reviewers significantly improved the manuscript.

AUTHOR DECLARATIONS

Conflict of Interest

The authors have no conflicts to disclose.

DATA AVAILABILITY

The data that support the findings of this study are openly available in Zenodo at https://doi.org/10.5281/zenodo.6497181, reference number 6497181.

REFERENCES

Baud, P., Schubnel, A., and Wong, T.-f., "Dilatancy, compaction, and failure mode in Solnhofen limestone," J. Geophys. Res. **105**, 289–303, https://doi.org/10.1029/2000jb900133 (2000).

Birch, F., "The velocity of compressional waves in rocks to 10 kilobars: 1.," J. Geophys. Res. **65**, 1083–1102, https://doi.org/10.1029/jz065i004p01083 (1960).

Blacic, J. D. and Hagman, R. L., "Wide-band optical-mechanical system for measuring acoustic emissions at high temperature and pressure," Rev. Sci. Instrum. **48**, 729–732 (1977).

Bridgman, P. W., "The technique of high pressure experimenting," Proc. Am. Acad. Arts Sci. **49**, 627–643 (1914).

Burdette, E., Kidder, S. B. K., and Hirth, G., "Laser displacement sensing for rock deformation: A Griggs internal load cell application," in *AGU Fall Meet. 2021* (AGU, 2021).

Burlini, L., Vinciguerra, S., Di Toro, G., De Natale, G., Meredith, P., and Burg, J.-P., "Seismicity preceding volcanic eruptions: New experimental insights," Geology **35**, 183–186 (2007).

Caristan, Y., "The transition from high temperature creep to fracture in Maryland diabase," J. Geophys. Res. **87**, 6781–6790, https://doi.org/10.1029/jb087ib08p06781 (1982).

Chopra, P. N. and Paterson, M. S., "The experimental deformation of dunite," Tectonophysics **78**, 453–473 (1981).

Christensen, N. I., "Compressional wave velocities in rocks at high temperatures and pressures, critical thermal gradients, and crustal low-velocity zones." J. Geophys. Res. **84**, 6849–6858, https://doi.org/10.1029/jb084ib12p06849 (1979).

Edmond, O. and Murrell, S. A. F., "Experimental observations on rock fracture at pressures up to 7 kbar and the implications for earthquake faulting," Tectonophysics **16**, 71–87 (1973).

Ferri, F., Gibert, B., Violay, M., Schilling, F. R., and Cesare, B., "Electrical conductivity in a partially molten lower crust from laboratory measurements on xenoliths (El Hoyazo, SE Spain)," in *EGU Gen. Assem. 2009* (Copernicus, Vienna, 2009), p. 8038.

Fischer, G. J., "The determination of permeability and storage capacity: Pore pressure oscillation method," in *Fault Mechanics and Transport Properties of Rocks* (Elsevier, 1992), Vol. 51, pp. 187–211

Fischer, G. and Paterson, M. S., "Dilatancy during rock deformation at high temperatures and pressures," J. Geophys. Res. **94**, 607–617, https://doi.org/10.1029/jb094ib12p17607 (1989).

Fredrich, J. T., Evans, B., and Wong, T.-F., "Micromechanics of the brittle to plastic transition in Carrara marble," J. Geophys. Res. **94**, 4129–4145, https://doi.org/10.1029/jb094ib04p04129 (1989); arXiv:1011.1669v3.

Frost, H. J. and Ashby, M. F., *Deformation Mechanism Maps*, 1st ed. (Pergamon Press, 1982).

Ghaffari, H. O. and Pec, M., "An ultrasound probe array for a high-pressure, high-temperature solid medium deformation apparatus," Rev. Sci. Instrum. **91**, 085117 (2020).

Gleason, G. C. and Tullis, J., "A flow law for dislocation creep of quartz aggregates determined with the molten salt cell," Tectonophysics **247**, 1–23 (1995).

Gosman, A. L., McCarty, R. D., and Hust, J. G., "Thermodynamic properties of argon from the triple point to 300 K at pressures to 1000 atmospheres," in *Natl. Stand. Ref. Data Ser.* (U.S., Natl. Bur. Stand., 1969), Vol. 27.

Greenwood, J. A. and Williamson, J. B. P., "Contact of nominally flat surfaces," Proc. R. Soc. London, Ser. A **5** (1967).

Griggs, D. T., "Deformation of rocks under high confining pressures: I. Experiments at room temperature," J. Geol. **44**, 541–577 (1936).

Griggs, D., "Hydrolytic weakening of quartz and other silicates," Geophys. J. R. Astron. Soc. **14**, 19–31 (1967).

Handin, J., "An application of high pressure in geophysics: Experimental rock deformation," Trans. Am. Soc. Mech. Eng. **75**, 315–324 (1953).

Hansen, L. N., Kumamoto, K. M., Thom, C. A., Wallis, D., Durham, W. B., Goldsby, D. L., Breithaupt, T., Meyers, C. D., and Kohlstedt, D. L., "Low-temperature plasticity in olivine: Grain size, strain hardening, and the strength of the lithosphere," J. Geophys. Res.: Solid Earth **124**, 5427–5449, https://doi.org/10.1029/2018jb016736 (2019).

Hayward, K. S., Cox, S. F., Fitz Gerald, J. D., Slagmolen, B. J. J., Shaddock, D. A., Forsyth, P. W. F., Salmon, M. L., and Hawkins, R. P., "Mechanical amorphization, flash heating, and frictional melting: Dramatic changes to fault surfaces during the first millisecond of earthquake slip," Geology **44**, 1043–1046 (2016).

Heard, H. C., "Transition from brittle fracture to ductile flow in solenhofen limestone as a function of temperature, confining pressure, and interstitial fluid pressure," in *Rock Deformation*, edited by Griggs, D. T. and Handin, J., Mem. Geol. Soc. Am., **79**, 193–226 (1960).

Heard, H. C. and Carter, N. L., "Experimentally induced 'natural' intragranular flow in quartz and quartzite," Am. J. Sci. **266**, 1 (1968).

Hirth, G. and Tullis, J., "The brittle-plastic transition in experimentally deformed quartz aggregates," J. Geophys. Res.: Solid Earth **99**, 11731, https://doi.org/10.1029/93jb02873 (1994).

Holloway, J. R., "Research techniques for high pressure and high temperature," in *Res. Tech. High Press. High Temp.*, edited by Ulmer, G. C. (Springer, Berlin, Heidelberg, 1971), pp. 217–258.

Holyoke, C. W. and Kronenberg, A. K., "Accurate differential stress measurement using the molten salt cell and solid salt assemblies in the Griggs apparatus with applications to strength, piezometers and rheology," Tectonophysics **494**, 17–31 (2010).

Ismail, I. A., "Experimental studies of instabilities in rocks with particular reference to earthquake focal mechanisms," Ph.D. thesis, University College London, 1974.

Jackson, I., Paterson, M. S., Niesler, H., and Waterford, R. M., "Rock anelasticity measurements at high pressure, low strain amplitude and seismic frequency," Geophys. Res. Lett. **11**, 1235–1238, https://doi.org/10.1029/gl011i012p01235 (1984).

Jones, C., "An experimental study of the relationships between P wave velocity, acoustic emission and deformation in rocks under crustal conditions," Ph.D. thesis, University College London, 1989.

Kanaya, T. and Hirth, G., "Brittle to semibrittle transition in quartz sandstone: Energetics," J. Geophys. Res.: Solid Earth **123**, 84–106, https://doi.org/10.1002/2017jb014682 (2018).

Kirby, S. H. and Kronenberg, A. K., "Deformation of clinopyroxenite: Evidence for a transition in flow mechanisms and semibrittle behavior," J. Geophys. Res.: Solid Earth **89**, 3177–3192, https://doi.org/10.1029/jb089ib05p03177 (1984).

Moarefvand, A., Gasc, J., Fauconnier, J., Baïsset, M., Burdette, E., Labrousse, L., and Schubnel, A., "A new generation Griggs apparatus with active acoustic monitoring," Tectonophysics **816**, 229032 (2021).

Möllhoff, M. and Bean, C. J., "Validation of elastic wave measurements of rock fracture compliance using numerical discrete particle simulations," Geophys. Prospect. **57**, 883–895 (2009).

Murrell, S. A. F., "Brittle-to-ductile transitions in polycrystalline non-metallic materials," in *Deform. Process. Miner. Ceram. Rocks*, 1st ed., edited by Barber, D. J. and Meredith, P. G. (Unwin Hyman, London, 1990), Chap. 5, pp. 109–135.

Murrell, S. A., Meredith, P. G., Sammonds, P. R., Ayling, M. R., and Jones, C., "High temperature triaxial apparatus for acoustic measurements," in *Rocks at Great Depth* edited by Maury, V. and Fourmaintraux, D., Vol. I (Balkema, Rotterdam, 1989), pp. 291–296.

Paterson, M. S., "High-pressure, high-temperature apparatus for rock deformation," Int. J. Rock Mech. Min. Sci. Geomech. Abstr. **7**, 517–526 (1970).

Peterson, R. E., *Stress Concentration Factors: Charts and Relations Useful in Making Strength Calculations for Machine Parts and Structural Elements* (Wiley-Interscience, New York, 1974).

Paterson, M. S., "Rock deformation experimentation," in *The Brittle-Ductile Transition in Rocks* (American Geophysical Union, Washington, DC, 1990), pp. 187–194.

Pohrt, R. and Popov, V. L., "Normal contact stiffness of elastic solids with fractal rough surfaces," Phys. Rev. Lett. **108**, 104301 (2012).

Pyrak-Nolte, L., Cook, N. G., and Myer, L. R., "Seismic visibility of fractures," in Proceedings of the 28th symposium on rock mechanics, University of Arizona, Tuscon (Balkema, Boston, Mass, 1987), pp. 47–56.

Raleigh, C. B., "Mechanisms of plastic deformation of olivine," J. Geophys. Res. **73**, 5391–5406, https://doi.org/10.1029/jb073i016p05391 (1968).

Rutter, E. H., "The influence of temperature, strain rate and interstitial water in the experimental deformation of calcite rocks," Tectonophysics **22**, 311–334 (1974).

Schoenberg, M., "Elastic wave behavior across linear slip interfaces," J. Acoust. Soc. Am. **68**, 1516–1521 (1980).

Tullis, T. E. and Tullis, J., "Experimental rock deformation techniques," in *Geophys. Monogr. Ser.* (American Geophysical Union, 1986), Vol. 38, pp. 297–324.

Tullis, J. and Yund, R., "The brittle-ductile transition in feldspar aggregates: An experimental study," Int. Geophys. **51**, 89–117 (1992).

Violay, M., Gibert, B., Mainprice, D., Evans, B., Dautria, J. M., Azais, P., and Pezard, P., "An experimental study of the brittle-ductile transition of basalt at oceanic crust pressure and temperature conditions," J. Geophys. Res.: Solid Earth **117**, 1–23, https://doi.org/10.1029/2011jb008884 (2012).